THE ASTROPHYSICAL JOURNAL, 392:497–508, 1992 June 20

A COMPLETELY SAMPLED APERTURE SYNTHESIS MAP OF THE CO EMISSION IN M51

DAVID S. ADLER[1,2] K. Y. LO,[1] MELVYN C. H. WRIGHT,[3] GUSTAV RYDBECK,[4]
RAYMOND L. PLANTE,[1] AND RONALD J. ALLEN[5]

Received 1991 January 28; accepted 1991 December 26

ABSTRACT

Interferometric observations from the Berkeley-Illinois-Maryland Association millimeter interferometer are combined with single-dish observations from the Onsala Space Observatory to create high-resolution *fully sampled* maps of CO (J = 1–0) emission from two 2′ fields in the spiral galaxy M51. In previous interferometer CO maps of M51, $\geq$65% of the CO flux density in each field is missing but assumed to be uniformly distributed through the field of view. In contrast, our maps recover all of the flux density and show directly that 75% of the CO flux density from the inner few kiloparsecs of M51 come from the spiral arms. The CO arms are wider ($\lesssim$1.3 kpc) and more extended than the CO arms presented in previous interferometer maps. The CO arm is clumpy along the arm with a linear scale $\sim$1 kpc.

The average arm-to-interarm intensity contrast over the two fields is $\geq$4.6:1; peak arm-to-interarm CO integrated intensity contrasts of $\geq$20:1 are seen in the inner arms. Some large "clumps" of interarm CO emission are seen. Streaming motions of up to 70 km s^{-1} (in the plane of the galaxy) are seen in the arms; these motions are consistent with those expected from the spiral density wave theory.

Both the intensity contrast and streaming motions are consistent with numerical simulations which show that orbit crowding is the dominant physical mechanism for gathering the molecular clouds into the arms. Dissipative cloud-cloud collisions and gaseous self-gravity must be included in the numerical models to account for the observed clumpiness along the spiral arms.

Adopting the Galactic conversion ratio of H_2 to CO integrated intensity, we find that the inferred gas mass of the molecular cloud complexes in the spiral arms of M51 is systematically larger than the virial mass. An H_2-to-CO conversion ratio in the inner spiral arms of M51 2.5 times smaller than the Galactic value will correct the disrepancy.

Subject headings: galaxies: individual (M51) — galaxies: ISM — techniques: interferometric

1. INTRODUCTION

Because of its proximity and low inclination, the grand design spiral galaxy M51 is an ideal candidate for studies of galactic structure. By studying the distribution of the various phases of the interstellar medium (ISM), we hope to delineate the physical processes responsible for creating the observed distribution of young stars in the spiral arms. One of the basic questions is how the molecular gas is distributed relative to the observed spiral structure in the disk. The distribution has bearing on the formation and lifetimes of molecular clouds, and how spiral density waves mediate the formation of the young stars and H II regions which outline the spiral structure.

To resolve the molecular spiral structure in M51, observations with sufficiently high resolution are required. From observations of 45″ to 60″ resolution, Rickard & Palmer (1981) and Scoville & Young (1983) could not discern the molecular spiral structure, and could only determine that the CO flux fell off as a function of radius. Rydbeck, Hjalmarson, & Rydbeck (1985, hereafter RHR) were the first to infer the presence of molecular spiral structure in M51 by a deconvolution technique. They also detected streaming motions of the gas into the arms; these motions were similar to those found in spiral density wave models (Roberts 1969). Lo et al. (1987, hereafter L87) made the first high-resolution (6″) interferometric map of the inner 1′.5 of M51, which showed that the molecular gas was highly confined to the spiral arms. Vogel, Kulkarni, & Scoville (1988, hereafter VKS) also detected streaming motions in the spiral arms on their high-resolution map of several fields. Allen, Atherton, & Tilanus (1986) were the first to show that parts of the H I spiral arms in M83 are shifted downstream from the dust lanes, and correspond more closely with the H II regions; the shift has also been found in M51 (Tilanus & Allen 1989). Several interferometric projects have recently shown that the molecular arm is aligned with the dust lane, with the H I and Hα distributed downstream (VKS; Lo et al. 1989; Rand & Kulkarni 1990, hereafter RK). Finally, recent IRAM 30 m telescope CO (J = 2–1) maps of M51 with 12″ resolution also show strong molecular spiral structure (Guélin et al. 1989, hereafter G89; Garcia-Burillo & Guélin 1990, hereafter GBG).

While interferometers are ideal for achieving the required high resolution, all interferometer maps suffer from the "missing short spacing" problem. The antennas of an interferometer can be placed no closer than D apart to avoid possible collisions, where D is the diameter of the individual antenna. As a result, there is a region around the origin of the uv plane with a radius $\approx D/\lambda$ where the visibilities cannot be measured by the interferometer (because of the shadowing of one antenna by another; for basic principles of aperture synthesis, see, e.g., Thompson, Moran, & Swenson 1986). If the source has a lot of structure with angular sizes $\geq \lambda/D$, the visibility amplitudes will be large in exactly the region of the uv plane

[1] Department of Astronomy, University of Illinois, 1002 W. Green Street, Urbana, IL 61801.
[2] Present address: NRAO, P.O. Box 0, Socorro, NM 87801.
[3] Radio Astronomy Laboratory, University of California at Berkeley, Berkeley, CA 94720.
[4] Onsala Space Observatory, S-439 00, Onsala, Sweden.
[5] Space Telescope Science Institute, 3700 San Martin Drive, Baltimore, MD 21218.

which the interferometer cannot probe. This results in "dirty" maps in which large-scale structures have been filtered out and regions of negative intensity surround small-scale structure. Furthermore, given the typically low signal-to-noise ratio (S/N) in maps of CO emission from galaxies, the deconvolution process to derive the "clean" maps, which are the ones presented and used for analysis, requires close inspection and can be very subjective.

In practice, interferometers with 10 m diameter telescopes recover 35% or less of the total CO flux density (as determined by a single-dish telescope) within the primary field of view (L87; VKS; RK). The usual assumption is that the missing flux density is distributed uniformly throughout the field of view (L87). Thus, while interferometer maps reveal the peaks and ridges of the CO brightness distribution, such as those along the spiral arms, they do not show the extended structure. Statements about the CO distribution in the interarm regions of M51 are therefore usually based on "reasonable" assumptions.

The Berkeley-Illinois-Maryland Association Millimeter Array (BIMA) has 6 m antennas, so the extent of the "missing short spacings" is proportionally smaller and more of the total CO flux density is recovered compared with interferometers with 10 m antennas. Even so, to recover all of the missing flux density, the "missing short spacings" need to be restored. This can be achieved by deriving the necessary short spacings from measurements by a filled-aperture telescope with a diameter greater than the shortest spacing of the interferometer.

One method of partially correcting for the missing flux density entails the inclusion of the "zero-spacing" flux density in the interferometer visibilities (cf. L87). This method lifts the signal (and the noise) out of the negative "bowl" caused by the abrupt drop of the interferometer visibilities to zero inside the shortest observed spacing. However, this method yields just a zero-point shift in the maps and provides no information on the distribution of the missing flux. Since the distribution of CO in galaxies is not uniform (RHR; GBG), this method is not a reliable way to recover fully the missing flux density in M51. The validity of this method is further called into question by the fact that a uniform distribution of gas in a rotating system is not a source of uniform brightness across the field when viewed in a narrow range of velocity.

A map created with a large single-dish telescope that completely covers the region of the interferometer primary beam can be used to recover the missing flux density. Short-spacing visibilities can be created from these single-dish data and included with the interferometer visibilities. This method has been used on Galactic sources (HCO^+ in IRc2, Vogel et al. 1984; CS in IRc2, Mundy et al. 1986) and extragalactic sources (H I in M101, Allen & Goss 1979). In this paper we use this method to make a fully sampled map of the CO distribution in M51.

In § 2 we summarize the procedure used to produce the combined interferometer and single-dish maps. Section 3 presents an analysis of the percentage of flux density recovered in the "interferometer-only" and in the "combined" maps. Section 4 presents the results derived from the combined map. In § 5 we analyze and discuss the implications of the results of the combined map. We summarize our conclusions in § 6.

2. COMBINING THE INTERFEROMETRY AND SINGLE-DISH MAPS

To obtain fully sampled CO maps in M51, we combined the short-spacing visibilities derived from observations using the Onsala Space Observatory (OSO) 20 m telescope with the visibilities of two fields in M51 using BIMA. The half-power primary beamwidth (FWHM) of BIMA is 110″ at 115 GHz. Eighteen different baselines ranging from 8 to 73 m provide a relatively uniform *uv* coverage and a synthesized beam of 7″ × 11″ (350 pc × 550 pc at a distance of 9.6 Mpc). 3C 273 was the primary amplitude calibrator; its amplitude was calibrated using observations of planets. The uncertainty in the flux density scale is on the order of 10%. 3C 273 and 3C 345 are used as the phase calibrators. The rms phase scatter is typically on the order of 0.3–0.4 radians for all baselines; this corresponds to positional errors of less than 1/12 of the synthesized beam, or less than 1″. The spectrometer was set up for maximum velocity coverage of 750 km s^{-1} (an effective bandwidth of 290 MHz), centered on $v_{LSR} = 470$ km s^{-1} with a resolution of 3.25 km s^{-1}. The data were velocity-averaged to a resolution of 10.4 km s^{-1} before the channel maps were produced using natural weighting in the spatial transform. Mapping of additional fields will proceed after the upgrade of the BIMA array. Adler, Lo, & Allen (1990) presented preliminary results on two additional fields to the north and west of the two in this survey; more data are needed to increase the signal-to-noise ratio in those two fields.

Single-dish spectra of the CO ($J = 1$–0) line from M51 were obtained using the OSO 20 m millimeter-wave telescope (RHR; Rydbeck et al. 1989, hereafter RHWR), with a FWHM of 33″. Spectra were obtained at points 15″ apart, although some regions are sampled at a spacing of 11″. An area larger than the two 2″ fields was mapped. Pointing uncertainties of 4″–6″ are reported for the single-dish data by RHR; since the single-dish map will contribute predominantly large-scale structure to the combined maps, these uncertainties should not significantly affect our results. The method used to combine the single-dish and interferometer data is similar to that described by Vogel et al. (1984). The single-dish data were first interpolated to a velocity resolution of 10.4 km s^{-1} to be consistent with the BIMA data. Irregularities in the spatial sampling of the single-dish data were interpolated to an 11″ interval using the CLEAN algorithm. Figure 1 shows the interpolated image at 20.8 km s^{-1} intervals.

To convert the units of the single-dish data from antenna temperature (T_A^*) to the units of the interferometer (Jy $beam^{-1}$), we use

$$S_\nu = \frac{2k}{\lambda^2}\,\Omega_b\,T_{mb}\,, \tag{1}$$

where

$$T_{mb} = \frac{T_A^*}{\eta_{mb}} \tag{2}$$

and

$$\Omega_b = \frac{\pi}{4\ln 2}\,\theta_{min}\,\theta_{maj}\ ; \tag{3}$$

η_{mb} is the main-beam efficiency of the 20 m telescope at 115 GHz, taken as 0.3 (RHR). Ω_b is a Gaussian approximation to the Onsala beam. For a beam size of 33″, the scaling factor is calculated to be $S_\nu/T_A^* = 39$ Jy K^{-1}.

The single-dish maps are first CLEANed to interpolate missing pixel values in the Onsala map, and to replace the actual beam by a Gaussian (there are no missing pixels in the two fields studied here). Since CLEAN works on the peaks in the maps, and the peaks are generally well represented by a

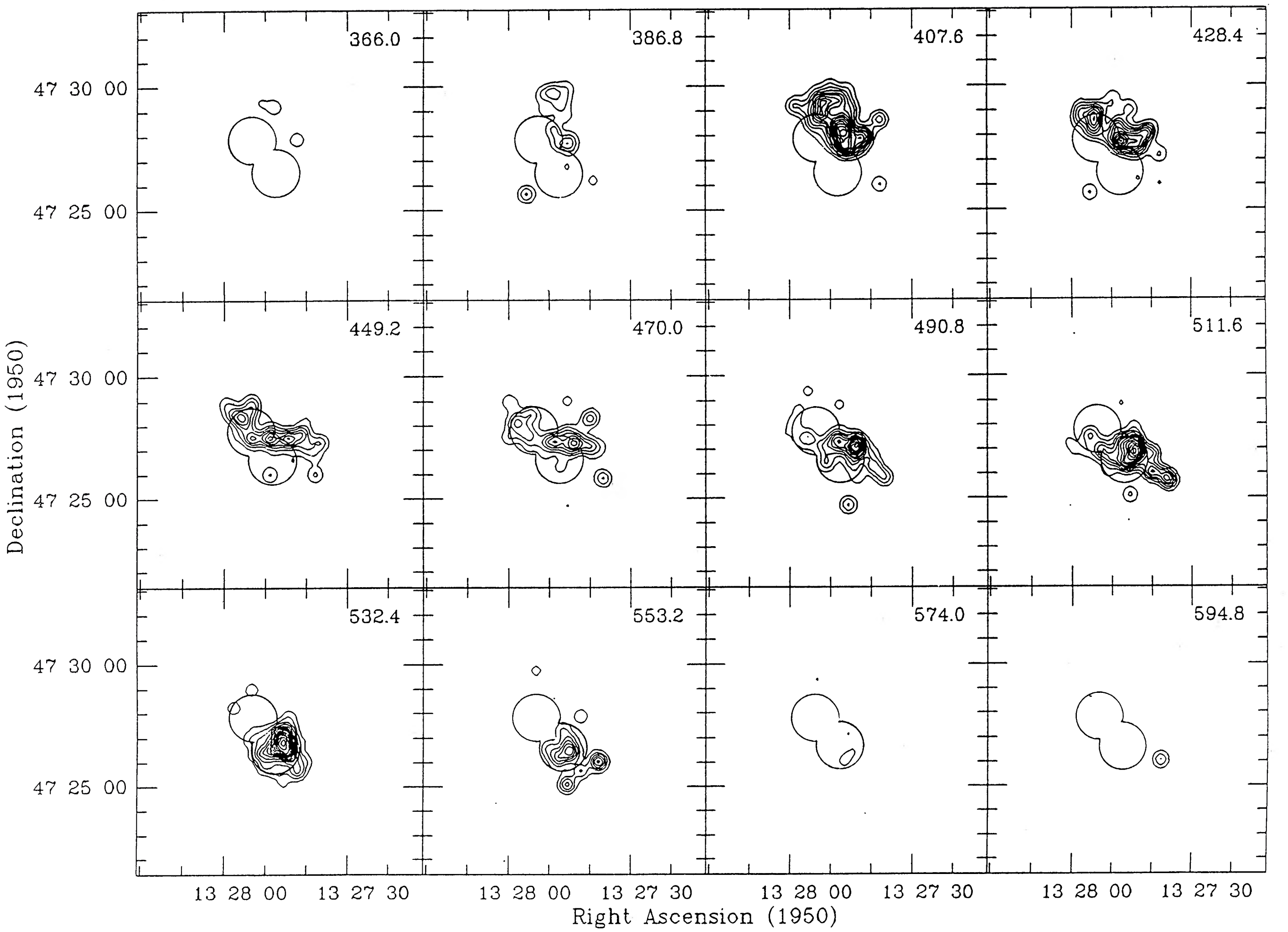

FIG. 1.—Onsala single-dish maps for the region covering the two interferometer fields. The contours are in units of main-beam temperature; the lowest contour is 0.001 K, with each successive contour increased by 0.001 K. The FWHMs of the two interferometer fields are superposed. The data were averaged in 10.4 km s^{-1} bins; every other channel is displayed.

Gaussian, approximating the Onsala beam by a Gaussian is adequate despite the 30% main-beam efficiency. The single-dish maps were then deconvolved by dividing their Fourier transforms by the Fourier transform of the Onsala beam (assumed to be Gaussian) and multiplying by the BIMA primary beam. These deconvolved maps were then used to compute the visibility along chosen (u, v) tracks in the aperture plane (*uv* plane). The phase centers of the single-dish and interferometer fields were not the same, so a phase shift was introduced in the Onsala data to account for the difference.

Since the Onsala data sample the visibility out to 2.5 times the shortest spacing of the interferometer data, we can check the compatibility of the two data sets in the overlap region. Visibilities were generated from the Onsala (u, v) tracks that corresponded to the three shortest BIMA baselines. For all three baselines, amplitudes and phases plotted against hour angle show good agreement between the interferometer and single-dish visibilities. The velocity profiles also show very good agreement between the two data sets along the same (u, v) tracks. The single-dish and interferometer amplitudes typically agreed to about 20%. This indicates that the value used for the main-beam efficiency of the Onsala telescope is reasonably accurate. The phase agreement between the two data sets is typically better than a radian; this indicates positional uncertainties in the extended structures of about 2″.

The sampling of the single-dish (u, v) data was chosen to provide the combined synthesized map with a uniformly sampled aperture plane. A circular, 12 hr track at a spacing of 3 m sampled every 12 minutes with one point at 0 m provides the fully sampled aperture plane. Thus the resulting combined map actually consists of only a few percent of the data derived from the single-dish observations (but note the effect of this small amount of single-dish data, as noted in the next section). The resulting maps are dominated neither by the interferometer nor by the single-dish data sets.

3. COMPLETENESS OF THE INTERFEROMETER AND COMBINED MAPS

Figure 2 shows flux density as a function of velocity for the single-dish, interferometer, and combined data sets for fields 1 and 2. The interferometer and combined map flux densities are taken from the total CLEANed flux density from each channel; channels judged not to contain signal were not CLEANed and have been assigned a flux density of zero. The uncertainty in the quoted CLEANed flux densities is roughly ± 0.5 Jy. Since the interferometer and combined maps had not

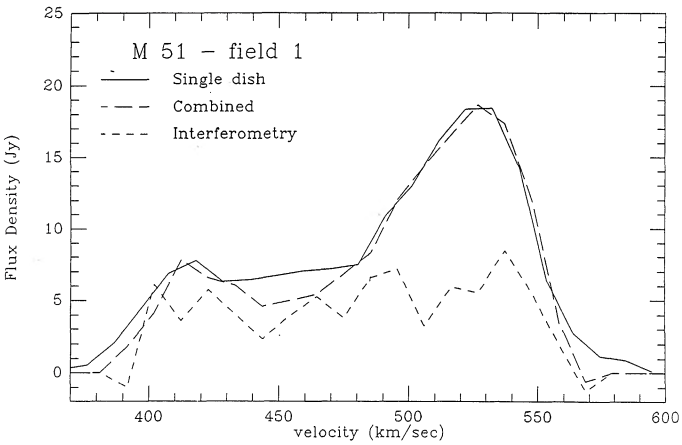

FIG. 2*a*

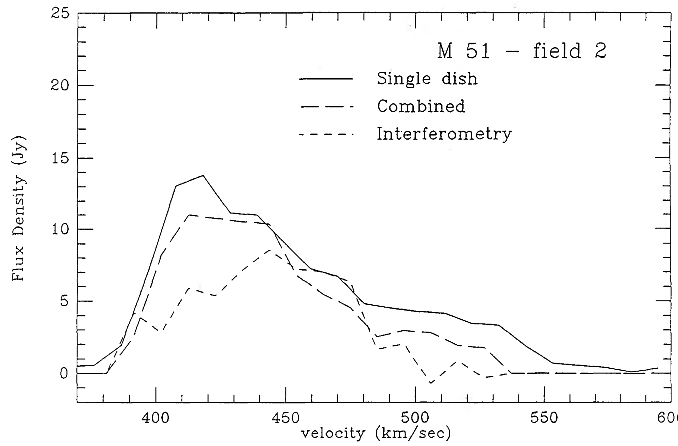

FIG. 2*b*

FIG. 2.—Total flux density per channel for the interferometer (*short-dashed line*), combined (*long-dashed line*) and single-dish (*solid line*) data cubes. (*a*) Flux densities for field 1; (*b*) flux densities for field 2.

been corrected for the primary-beam response, the single-dish maps were multiplied by the interferometer primary beam (again, assumed to be a Gaussian with FWHM = 110″) to make the results comparable. Table 1 shows the percentage of the single-dish flux density recovered by each of the interferometer and combined maps.

Even without single-dish data, the BIMA map recovers ≥50% of the total flux density. The high percentage of recovered flux density is not surprising considering the size of the antennas used. The 6 m BIMA antennas allow shorter spacings to be taken, which in turn recovers more flux than interferometers with larger antennas. In comparison, the Owens Valley Interferometers with 10 m antennas typically recovers 25%–35% of the single-dish flux density in M51 maps (L87; VKS; RK). One also expects to recover a high percentage of the flux density in the channels near the systemic velocity (470 km s^{-1}) due to the fact that emission near v_{sys} is restricted to a small solid angle on the sky along the minor axis.

4. RESULTS

4.1. *Integrated* CO *Intensity Map*

The integrated intensity and velocity distributions were estimated from the zeroth and first moments of the channel maps. The rms surface brightness noise level in individual channel maps is 0.25–0.30 Jy $beam^{-1}$; we used a cutoff of 0.3 Jy $beam^{-1}$ while making the moment maps. The velocity-integrated intensity maps were created with a Hanning smoothing over the 10.4 km s^{-1} velocity channels and a Gaussian smoothing over 10″ in space. The moment maps were then corrected for the primary-beam response and mosaicked together using a simple weighting technique that takes into account a cell's position relative to the pointing center of the field (Mundy et al. 1986; VKS).

TABLE 1

PROPERTIES OF THE MAPS

	Interferometer Map	Combined Map
Flux density recovered per channel	30%–85%	60%–100%
Total single-dish flux density recovered	50%	93%

It is useful at this point to note some limitations to this method when deriving velocity-integrated intensities. The integrated intensity maps presented here are not simple sums of the maps at each velocity bin (channel maps); this has not always been stated explicitly in the past. The integrated intensity maps are usually the "zeroth-moment" maps derived from the "masked moment" method which was originally developed for 21 cm H I maps of galaxies that also suffer from limited S/N. A simple sum of M channel maps will yield an integrated map with noise that has a variance $M\sigma^2$, the noise variance of each channel map. Since there is not usually signal in every channel at the same spatial location, the S/N of the summed map will be reduced from that of the individual channel maps.

Consider a data cube, $T(x, y, v_i)$, made up of the channel maps $T_i(x, y)$. The zeroth-moment map is calculated by

$$M_0(x, y) = \sum_i T_i(x, y) , \quad (4)$$

but the inclusion of $T_i(x, y)$ *in the sum depends on a conditional test.* $T_i(x, y)$ is included in the sum if $\langle T_i(x, y)\rangle$ is greater than a threshold value, usually set about equal to σ. $\langle T_i(x, y)\rangle$ is the averaged value of $T_i(x, y)$ in a small volume around the pixel (x, y, v_i) that should contain more than one resolution element in the spatial and velocity dimensions. Both the threshold value and the volume are specified inputs to the moment calculation. This conditional test tends to exclude from the zeroth-moment map pixels that contain noise *and* pixels that contain low-level signal with magnitudes comparable to the noise. *The noise statistics in such a moment map are thus no longer straightforward.*

The integrated intensity maps are presented in Figures 3 (interferometer only) and 4 (combined). The peaks in the two maps are generally the same size, shape, and intensity. The majority of the recovered flux density in the combined map is found in the arms, making them wider and more extended (see next section). Some interarm emission is seen, the most striking example being in field 2, but overall *the combined map does not show a significant amount of interarm emission.*

It is interesting to note the effects on the width and extent of the molecular arm as a higher percentage of the total flux density is recovered. GBG have pointed out that their broad molecular arm does not appear in the RK map because of the missing short spacings in the interferometer survey. By com-

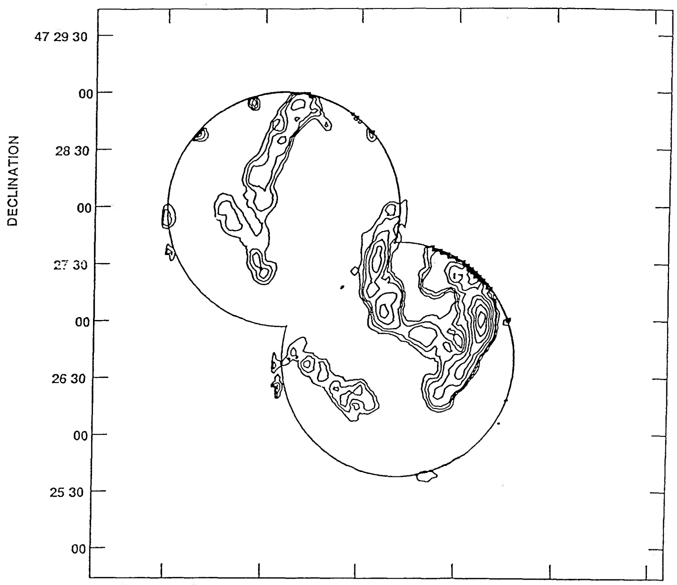

FIG. 3.—Velocity-integrated interferometer map for fields 1 and 2. The mosaicking method is described in § 2. Contour levels are at 10, 20, 30, 50, 70, 90, 110, 130, and 150 Jy beam^{-1} km s^{-1}. The rms noise in the map is 7.5 Jy beam^{-1} km s^{-1}. The FWHMs of the two fields are superposed.

paring maps that recover 25%–30% of the total flux density (L87; VKS; RK), 50% (Fig. 3), and 100% (GBG; Fig. 4), the molecular arm is seen to get wider and more extended. The amount of interarm emission does not appear to increase by a significant amount. It thus appears that the "missing" flux density in interferometer surveys of M51 *is not* spread uniformly through the field of view, as previously believed (L87; VKS; RK).

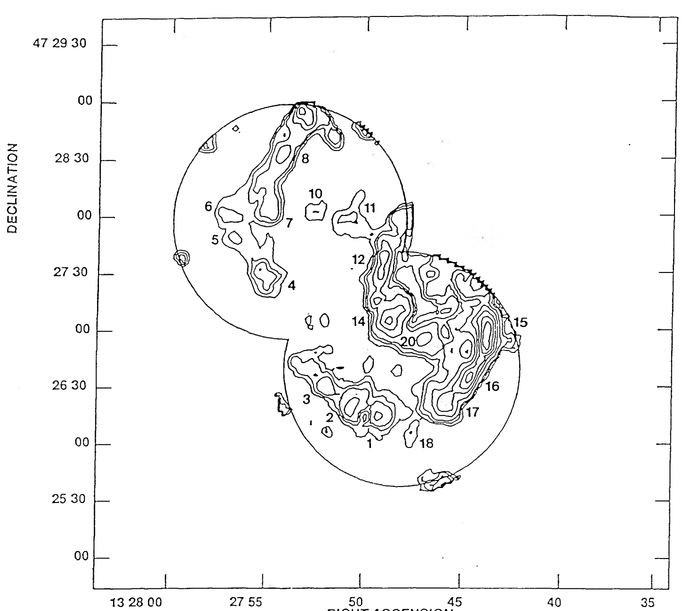

FIG. 4.—Velocity-integrated combined map for fields 1 and 2. Contour levels are the same as in Fig. 3.

4.2. *Arm-to-Interarm Contrast: Total Flux Density of* CO *Emission*

The relative amounts of CO emission from the spiral arm versus the interarm regions are relevant to a number of issues. Inspection of the individual channel maps from the interferometer and combined data cubes indicates that there is little extended emission in the interarm region and that most of the recovered flux density is found in the arms. To check directly where the missing flux density originates, we compare the distribution of CO emission at each velocity in the combined map to that in the interferometer map.

Figures 5*a* and 5*b* show the interferometer and combined maps at 516 km s^{-1} in field 1. At this velocity the interferometer recovers 35% of the total single-dish flux density (see Fig. 2*a*). The arms in the combined map are seen to be wider and more continuous than the interferometer map. Figures 6*a* and 6*b* show the interferometer and combined maps at 485 km s^{-1} in field 1. The interferometer recovers 80% of the total single-dish flux density at this velocity. Figure 6 shows that the signal is generally confined to the same region in both maps: the arm segments are the same width, while the combined map has slightly more emission in the peaks of the southern arm. The two examples show that *there is not a significant increase in the amount of interarm emission in the combined map.* The majority of the flux density recovered in the combined map is restricted to the regions of the spiral arms.

Another way to demonstrate this is to determine the percentage of the flux density found in the interarm regions. Using the velocity-integrated intensity map (Fig. 4) as a guide to the location of the arms, we calculated the amount of interarm flux density in each of the channel maps of the CLEANed data set (i.e., before the zeroth-moment map cutoffs were made). For the two fields, between 22% and 27% of the total flux density lies in the interarm region, which covers about 75% of the total area of the surveyed fields. If this emission is spread uniformly through the interarm region and has a width of 40 km s^{-1}, the average flux density would be 0.1 Jy beam^{-1}, well below our rms noise level of 0.2–0.3 Jy beam^{-1} for the channel maps. (1 Jy beam^{-1} corresponds to 0.88 K, which is the equivalent Rayleigh-Jeans brightness temperature averaged over the beam size, $\sim$350 pc $\times$ 550 pc). This would explain the apparent lack of interarm emission in the integrated intensity map, which was created using a cutoff of 0.3 Jy beam^{-1}. The two large interarm features in field 2 take up approximately 10% of the total interarm flux density.

4.3. *Size Scales of the* CO *Emission*

The most striking difference between our combined map and previous interferometer maps (including the one in this study) is the width of the spiral arms. Previous interferometer maps of M51 have quoted arm widths of 10″–20″, corresponding to less than 1 kpc at a distance of 9.6 Mpc (VKS: 300 pc; RK: 400–900 pc; L87, OVRO: 700 pc; Lo et al. 1989, BIMA: 1 kpc). The combined map in this survey has arms that range from 15″ to 28″ wide (at 20% of the maximum), corresponding to arms of up to 1.3 kpc in width. This is in good agreement with the single-dish study of GBG.

The arms are not smooth and uniform but exhibit a rather clumpy nature. The clumps are spaced about every 20″ (about 1 kpc) along the arms. It is also apparent that much of the molecular mass in the arms is tied up in these objects. The majority (17 of 21) of the clumps of CO emission are resolved. The extent of a clump is taken at the FWHM intensity and

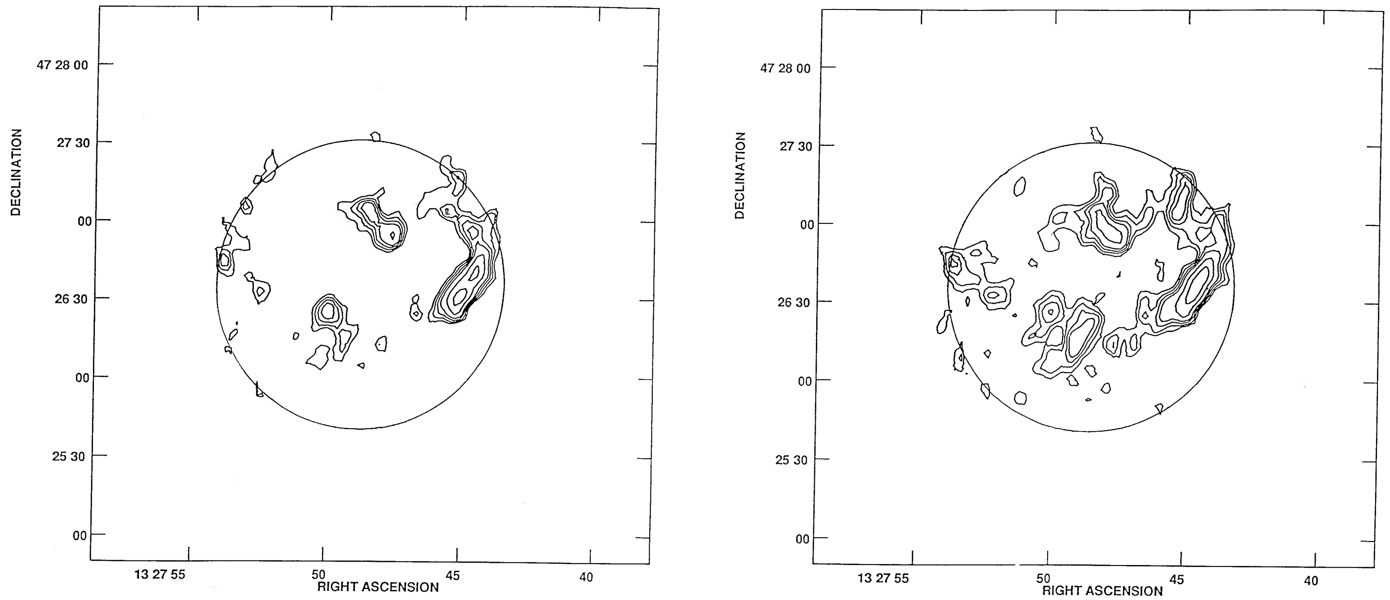

FIG. 5a FIG. 5b

FIG. 5.—Channel maps in field 1 at 516.4 km s^{-1} for (*a*) the interferometer and (*b*) the combined data cubes. Contours are at 0.4, 0.6, 0.8, 1.0, 1.4, 1.8, 2.2, and 2.6 Jy beam^{-1}. The noise level in each map is 0.3 Jy beam^{-1}. The FWHM of 110″ is superposed.

deconvolved with the beam to produce a clump size. The clumps are typically 300–800 pc, much larger than the individual giant molecular clouds (GMCs) in our Galaxy. They have been called giant molecular complexes (L87) and giant molecular associations (GMAs; VKS). Henceforth we will call such a complex a GMA.

4.4. *Comparison with Other* CO *Maps of M51*

The majority of the peaks in the combined map (Fig. 4) correspond in position to the peaks in the interferometer map (Fig. 3). The region of overlap between the combined map and the map of GBG shows good agreement in the position and shape of the peaks. In fact, the two interarm GMAs in field 2 correspond in position to one of the "bridges" seen in the GBG CO ($J = 2$–1) maps. The peaks detected in the inner arm by L87 with OVRO agree in position and intensity with the peaks in the overlap region of the combined map. Therefore, we have some independent confirmation that the combined map is correct.

Many of the peaks in the combined map agree with the giant molecular associations in the RK map, but there are some discrepancies. There is general agreement in the overlapped region of the two maps, except for some regions. RK have a large arm segment extending from $\alpha = 13^{\mathrm{h}}27^{\mathrm{m}}54^{\mathrm{s}}$ to

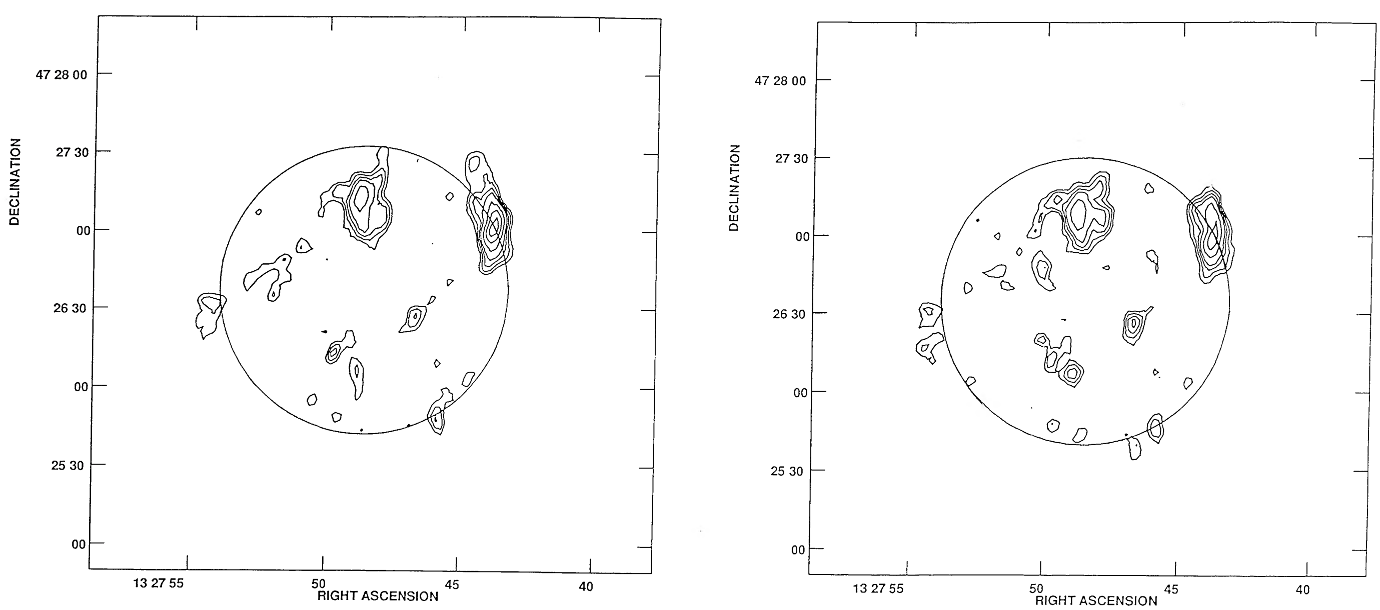

FIG. 6a FIG. 6b

FIG. 6.—Channel maps in field 1 at 485.2 km s^{-1} for (*a*) the interferometer and (*b*) the combined data cubes. Contours and noise levels are the same as in Fig. 5.

$\alpha = 13^h27^m56^s$ and $\delta = 47° 27' 00''$ to $\delta = 47° 27' 30''$, with no emission north of that until the beginning of the northeastern arm at $\delta = 47° 28' 00''$. In contrast, both figures 3 and 4 show no emission in that range, with the northeastern arm starting at $\delta = 47° 27' 15''$. In both instances, the emission in question is near the edge of a beam. This may reflect the problems of the typically low signal-to-noise ratios in extragalactic observations. Another difference between the two maps is that the majority (16 of 26) of the RK complexes are unresolved, while almost all of the GMAs (17 of 21) in our survey are resolved. The difference in the number of resolved GMAs in the two surveys is due to the fact that the combined map (Fig. 4), which recovers almost all of the total flux density, has wider arms and hence larger GMAs than the RK survey.

The combined map makes detection of strong interarm emission in M51 possible. The lower rms noise level of the RK map (2–4 Jy beam^{-1} km s^{-1}) allows the detection of interarm clumps that are below our rms noise level (7.5 Jy beam^{-1} km s^{-1}). We do find a correlation between the position of some of the interarm emission in Figure 4 and the RK map, but most of their interarm GMAs fall outside the field of view of our combined map. Their GMA I7 falls in the vicinity of the interarm emission in field 2 of Figure 4; the peak positions are different by 20″. Their I3 corresponds to a clump just outside the FWHM of field 1 in Figure 4; I6 is within 10″ of another large clump also on the edge of the beam. No emission is seen near their I1 and I2 GMAs; a fairly sizeable clump on the southern edge of field 1 in the combined map does not correspond to any RK interarm emission. Completion of fields to the north and west of the galactic center will allow for a more complete analysis of the interarm emission.

There are also some discrepancies between the intensity of the peaks of our interferometer map (Fig. 3) and that of RK. Since BIMA recovers roughly twice the flux density of OVRO for the M51 maps, it is expected that the intensities of Figure 3 will be somewhat higher than those of RK. However, since most of the missing flux density contributes to widening and extending the arms (§ 3), the *peak* intensities should not be significantly higher. Nevertheless, six of the GMAs in the inner eastern arm and southern arm of Figure 3 have intensities that are a factor of 2 brighter than the equivalent GMAs in RK. Three GMAs in the western arm of Figure 3 have intensities over 4 times higher than the equivalent GMAs in the RK map. Clearly, these discrepancies in the small-scale features recorded by the two instruments cannot be entirely attributed to the different percentages of recovered flux density or to the differences in sensitivity in the two maps.

4.5. *Complexes of Molecular Clouds: Sizes, Masses, Boundedness*

As indicated in § 3.3, the GMAs in our maps are resolved by our synthesized beam, in contrast to RK. The equivalent Rayleigh-Jeans brightnesses of the GMAs are typically ≤ 4.5 K, averaged over the 350 pc × 550 pc beam. If the brightness temperature of the individual clouds is similar to that of Galactic GMCs (~ 10 K), the area filling factor is then 0.5 or less. Higher resolution is clearly needed to resolve the individual clouds in the GMA.

The calculation of the molecular mass in the GMAs requires the assumption of the conversion ratio between the observed integrated CO intensity and the molecular hydrogen column density, $X = N(H_2)/I_{CO}$, which is not determined for M51. The usual working assumption is that the same conversion ratio determined for the Galactic disk (Scoville & Sanders 1987) can be applied. The problems associated with this approach have been reviewed extensively (see Maloney 1990). The working assumption is probably appropriate when applied to regions with physical conditions similar to those of the Galactic disk, and is useful for comparative purposes. In this paper we adopt $X = 3$, in units of 10^{20} cm^{-2} (K km sec^{-1})$^{-1}$, the same X-value as used by RK (but see Solomon et al. 1987 or MacLaren, Richardson, & Wolfendale 1988 for discussions of the variation in recent derived values of the Galactic conversion ratio).

The GMA size (taken as the geometric mean of the width on the right ascension and declination axes), the mass of molecular hydrogen [$M(H_2)$], the full width at half-maximum intensity of the CO emission corrected for instrumental resolution (ΔV), the measured integrated intensity (I_{CO}), and the total mass of the GMAs using the virial theorem (M_{vt}; see below) are listed in Table 2. The molecular hydrogen masses are much greater than the masses found for Galactic molecular clouds (typically 10^5 to a few times 10^6 $M_\odot$: Solomon et al. 1987; Scoville et al. 1987; Dame et al. 1986). Part of this difference is due to selection effects; we are obviously not detecting the fainter, less massive clouds in M51 owing to our limits in sensitivity. Our linear resolution is also much lower than that for Galactic surveys; many of the GMAs will presumably break up into smaller, separate entities when observed with higher resolution.

For a spherical cloud with a density law of $\rho \propto r^{-1}$, the virial mass can be written

$$M_{vt} = 190R\,\Delta V^2 \tag{5}$$

(MacLaren et al. 1988), where R is the radius of the cloud. This expression assumes that the gas cloud is in a steady state, and leaves out effects due to the magnetic fields (see Lo 1991). Again, this is consistent with the expression used by RK. Uncertainties in the measurements of R and ΔV, estimated to be 20% for both, would lead to uncertainties in M_{vt} of about

TABLE 2

GMA PROPERTIES

GMA	D[a] (pc)	I_{CO} (Jy beam^{-1} km s^{-1})	$M(H_2)$[b] (10^7 $M_\odot$)	ΔV[c] (km s^{-1})	M_{vt}[d] (10^7 $M_\odot$)
1	312	58.33	2.5	23.8	1.7
2	589	60.42	9.3	18.4	1.9
3	373	45.13	2.8	29.1	3.0
4	463	52.15	5.0	45.2	9.0
5	419	25.05	2.0	21.6	1.8
6	532	24.64	3.1	10.0	0.5
7	617	40.59	6.9	23.4	3.2
8	300	66.31	2.6	26.9	2.0
10	315	20.38	0.9	26.9	2.1
11	630	25.04	4.4	18.0	2.0
12	547	88.29	11.7	45.2	10.6
14	695	96.78	20.8	37.6	9.3
15	670	144.23	28.8	41.0	10.7
16	533	118.80	15.0	30.8	4.8
17	557	87.60	12.1	28.2	4.2
18	329	21.50	1.0	16.5	0.9
20	814	56.59	16.7	34.3	9.1

[a] Geometric mean of the deconvolved GMA widths (in R. A. and decl.).
[b] $M(H_2) = XI_{CO}$(K km s^{-1}) × A(pc^2), for $X = X_{Gal}$. 1 Jy beam^{-1} = 0.88 K.
[c] Line width deconvolved for velocity resolution (10.4 km s^{-1}).
[d] $M_{vt} = 190R\Delta V^2$.

50%. Including the uncertainty of the assumed density law of the cloud would make the uncertainty in M_{vt} larger.

It is also useful to consider what the ΔV we measure represents and what the derived M_{vt} means. Since it is unlikely that the beam is filled with a single massive cloud (the beam size in the current survey would correspond to a cloud of over 500 pc in diameter), the ΔV we measure is indicative not only of the internal motions within a single cloud, but also a cloud-to-cloud random motion of the clouds that make up the GMA. Since M51 is virtually face-on, the ΔV we measure will be primarily the z-component of the velocities involved.

Given the present resolution, these two components cannot be separated. If the observed ΔV is dominated by the cloud-to-cloud random motion, which is presumably responding to the total mass density in the galactic disk, then the virial mass based on ΔV will include the mass of other components besides molecular hydrogen inside the GMA. For example, if we assume that the internal velocity dispersion of the clouds is 4 km s^{-1}, then the observed ΔV of 20–45 km s^{-1} implies a cloud-to-cloud velocity dispersion in the z-direction of 7.5–19 km s^{-1}. This implies either a large z-scale height of the molecular layer or a large mass density in the disk. For comparable numbers in the solar neighborhood see Bahcall (1984) and Sanders & Scoville (1984). The mean stellar density at the mid-plane of the disk in the solar neighborhood is 0.05 $M_\odot$ pc^{-3} (Bahcall 1984), so that the stellar mass enclosed within a molecular cloud is small compared with the gas mass. However, at regions close to the nucleus or where the stellar density is several $M_\odot$ pc^{-3}, i.e., approaching the mean gas density in a molecular cloud, the virial mass will significantly overestimate the gas mass.

4.6. *Comparison of Molecular Mass and Virial Mass*

RK compared the virial mass for the GMA with their molecular hydrogen mass (including helium) to determine whether the GMA is gravitationally bound. We make the same comparison from our mass calculations (Fig. 7). Our higher integrated intensities, along with the larger (resolved) cloud sizes, contribute to make our molecular masses higher by a factor of 2–3 than the RK masses. Since we used the same form of the virial theorem as did RK, our virial masses are generally quite similar. Figure 7 shows clearly that our inferred total gas mass [$1.36M(H_2)$, to correct for helium abundance of 9% by number] is consistently larger than the virial mass, even allowing for the uncertainties involved. This is of course a physically impossible result. To insist that $1.36M(H_2)$ equals M_{vt} within the errors, we would have to adopt $X = 1.2$, a value 2.5 times smaller than the Galactic value.

Recent observations of external galaxies have shown evidence for conversion ratios different from the Galactic value. A similar comparison of the total gas mass and virial mass of molecular clouds in the Large Magellanic Clouds led to an X that is $\sim$6 times larger than the Galactic value (Cohen et al. 1988; Johansson 1990). Wilson & Scoville (1990) in a similar exercise found that with the Galactic conversion ratio, the two masses are comparable for the molecular clouds detected in their interferometer maps of M33, which constitute 30% of the total CO flux. A recent survey of the SMC by Rubio et al. (1991) shows that the conversion ratio is $\sim$20 times larger than the Galactic value. Planesas, Scoville, & Myers (1991) point out that in the nucleus of the starburst galaxy NGC 1068, a conversion ratio of $0.25X_{Gal}$ could be used to account for the higher gas temperatures (assuming similar densities) in the region. The above results and the result in this paper indicate that the conversion ratio may vary depending on the physical conditions in which the molecular clouds find themselves. It should also be noted that sources of error in the calculation of the conversion ratio arise from uncertainties in the density distribution of the GMA (since the constant in eq. [5] depends on the assumed density law; see MacLaren et al. 1988) and the distance to the galaxy [since $M_{vt} \propto D$ and $M(H_2) \propto D^2$]. Clearly, more studies are needed and direct determinations of the gas density and temperature are necessary to confirm this excitation effect.

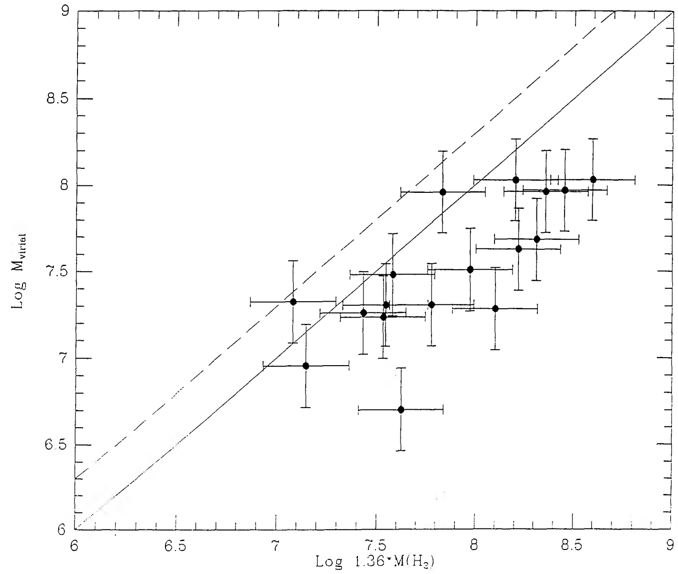

FIG. 7.—Comparison of the derived total mass [$1.36M(H_2)$ to correct for the helium abundance] with the virial mass. The solid line corresponds to $M_{CO} = M_{vt}$, the dashed line to $M_{CO} = \frac{1}{2}M_{vt}$ (i.e., where $E = 0$, with the GMA being "marginally bound"). The error bars correspond to the measurable quantities only; systematic quantities (distance, conversion ratio, cloud density structure) are not included, since they affect each GMA proportionally.

4.7. *Arm-to-Interarm Contrast; Integrated Intensity of CO Emission*

Numerical simulations of spiral galaxies show that a spiral density wave can efficiently gather molecular clouds into the arm regions (Roberts & Hausman 1984, hereafter RH; Roberts & Adler 1989). Therefore, an observational indicator of the presence (or lack) of a density wave is the amount of gas found in the region of the spiral arms. The degree of concentration of gas in the arms thus depends on the strength of the density wave, as well as the cloud-to-cloud velocity dispersion. This concentration of gas to the arms is usually expressed as an *average* arm-to-interarm intensity contrast. This ratio is often given as a single number: an intensity averaged over an entire arm or arm segment compared with a large section of interarm emission. The degree of clumpiness in the arms can be expressed through a *peak* arm–to–average-interarm intensity contrast; this number is often useful because averages over large areas can hide the clumpy nature of the emission.

Figure 8 shows the azimuthal variation of I_{CO} at radii of 1.75, 1.95, 2.15, and 2.40 kpc. While the plots are not completely independent (the spacing of $\sim$200 pc corresponds to roughly half of the synthesized beamwidth), they serve as a useful illustration of the relative amounts of arm and interarm emission. The CO arms stand out quite clearly, and it is

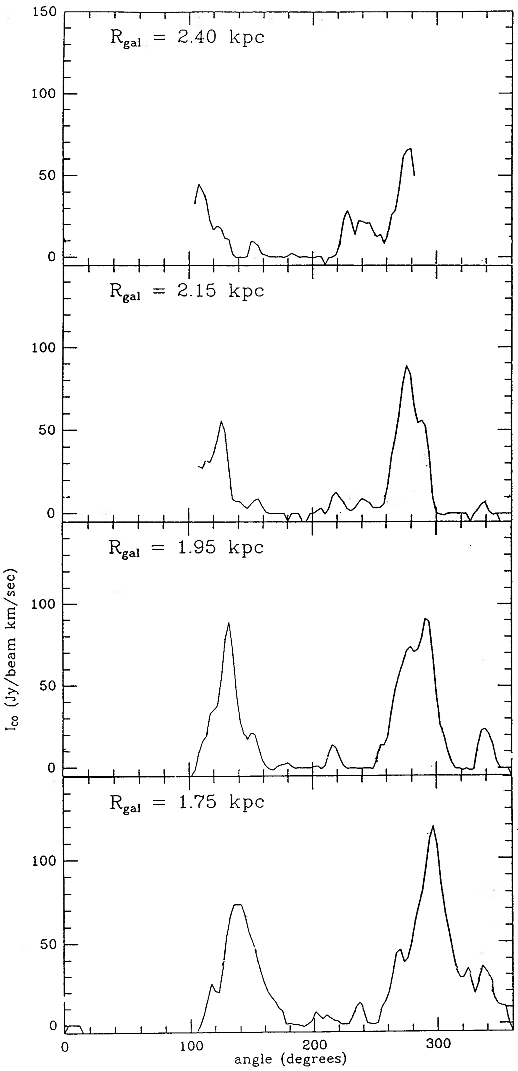

FIG. 8.—Azimuthal distribution of I_{CO} at galactocentric radii of 1.75, 1.95, 2.15, and 2.40 kpc (assuming a distance of 9.6 Mpc), taken from Fig. 4. The linear spacing between plots corresponds to roughly half of the synthesized beamwidth. The I_{CO} azimuthal distribution is limited by the field of view, as seen in Fig. 4. Zero degrees is defined as directly west of the center of the galaxy; increasing angle corresponds to counterclockwise rotation in Fig. 4. The transition of upstream to downstream occurs from left to right in this figure.

evident that the majority of detectable interarm emission is restricted to a few isolated clumps. We calculate the average arm-to-interarm intensity contrast for the different arm segments in Figure 4. Using the map noise level (7.5 Jy beam^{-1} km s^{-1}) to represent the average interarm emission, we get average intensity ratios of $\geq 6.3:1$ for the inner western arm; $\geq 5:1$ for the inner eastern arm, and $\geq 3.5:1$ for the outer arm segments. The average arm-to-interarm intensity ratio over the entire map is $\geq 4.6:1$. If the conversion ratio between CO intensity and H_2 column density is the same for spiral arms and interarm regions, these average CO intensity ratio lower limits can be compared with surface density ratios derived from spiral density wave models (3:1–8:1; RH, Roberts & Adler 1989). These ratios are consistent with a recent IRAM CO (J = 2–1) survey (at 12″ resolution) of the western part of M51 (G89; GBG).

The peak arm emission is seen to be quite high above the interarm emission; again using the noise level of the map to represent the interarm emission, we get a lower limit to the peak arm-to-interarm intensity contrast of $\geq 16:1$. Peaks in the inner arms get as high as 20:1. For the western arm (the same as in our map), GBG obtain peak arm-to-interarm intensity contrasts of 10:1–17:1, with lower values in the outer arm, consistent with our results.

These high peak arm–to–average-interarm contrasts become evident primarily because the high angular resolution of the maps allows resolution of the arm and interarm regions. CO maps of M51 with low resolution show little or no density contrast between the arms and interarms (Rickard & Palmer 1981, FWHM = 65″; Scoville & Young 1983, FWHM = 50″; RHR FWHM = 33″). Verter & Kutner (1988) found a mean ratio of 4:1 in the southwest part of the disk in an NRAO CO (J = 2–1) 12 m survey (FWHM = 30″), and the deconvolved maps of RHWR revealed contrasts of $\geq 5:1$. This work and GBG present an extension of this trend. It should be noted that high peak arm-to-interarm intensity contrasts of this nature are not unheard of in other galaxies; the ratio is seen to be higher than 25:1 in M31 (Stark 1985). Studies of the large molecular complexes in the Galaxy show that most of the molecular mass is restricted to the spiral arm regions (Dame et al. 1986), which would also lead to a high arm-to-interarm ratio.

4.8. *Streaming Motion along the Spiral Arm*

One also expects the gas distribution to show certain velocity characteristics in the presence of a spiral density wave. In a plot of gas density (or intensity) as a function of distance across an arm, we expect to see a sharp rise in the intensity as the gas encounters the shock, followed by a slow decrease as the gas moves downstream through the arm into the interarm region. The tangential component of the gas velocity is also expected to show a steep dip at the point of the shock, while the radial velocity shows a less pronounced effect (see Fig. 4, RH).

The streaming motion of the gas in the arms is calculated using the peak v_{LSR} of the GMA. The rotational velocity is first calculated, after which a model rotation curve of the unperturbed velocity field (Tully 1974) is subtracted. This model has a rapid rise in velocity up to 220 km s^{-1} at 20″, after which the rotation curve remains flat at larger radii. Once the model is removed, streaming motions in the arm of up to ± 70 km s^{-1} are seen in the plane of the galaxy, in a direction consistent with that of density wave theory. This is consistent with the results of RHWR and VKS, as well as the Hα results of Tilanus & Allen (1991; see also Tilanus 1990).

However, we are unable to identify the sharp rise in surface density characteristic of a spiral density wave. The problem is mostly one of resolution; since our arms are about 20″ wide, we only get 2–3 beams across the arm. Although the velocity gradient is clearly seen, these three points are insufficient to detect the steep drop in velocity as the gas enters the arm. Higher resolution observations of some individual GMAs are needed to check for these properties.

5. DISCUSSION

5.1. *Physical Mechanisms of Confining GMA to Spiral Arms*

A detailed comparison between theory and the observations of gas flows in M51, similar to the studies carried out by Visser (1980a, b) in M81, would be desirable at this point. These comparisons require the determination of σ_i and v_i, the surface density and velocity distributions of component *i*. However, the observations of the multiple components of the ISM in M51 are not sensitive enough to map these distributions throughout the galaxy (see also Tilanus 1990). Nevertheless, numerical models can still shed some light on the physical processes occuring in the disk of M51.

The computational modeling of galactic systems requires the inclusion of various physical processes. With several processes competing to produce the resulting distribution of clouds in the model disk, it is often difficult to discern which process is responsible for the different characteristics of the disk. It is therefore useful to reduce the computational model down into its basic parts to study the effect of the addition of various physical processes one at a time. While the results of the current observational survey obviously cannot be stripped down in a similar way, the results can be used to place constraints on the parameters in the computational models.

It has been shown that the inclusion of an infinitesimally thin density wave shock—independent of the inclusion of cloud-cloud interactions or gaseous self-gravity—is enough to cause the strong pileup of gas in the arms (RH; Roberts & Stewart 1987, hereafter RS). This is due to the process of *orbit crowding*, where cloud orbits converge as they enter the potential minimum leaving the clouds to linger in the arms; as the clouds exit the arm, their orbits diverge naturally. Even a density wave of relatively low amplitude (a few percent over the background axisymmetric potential) is adequate to organize the clouds into the arms. Thus a molecular spiral arm can form in a spiral gravitational perturbation, even if there is no gravitational attraction or cloud coalescence between the clouds.

This is not to imply that orbit crowding alone can account for the appearance of the molecular emission in M51. Computational models run only with a spiral density wave show that the compression ridge of clouds in the arms "sloshes" back and forth in spiral phase across the shock region, never reaching a steady state (RS). While there is some clumping of clouds in the model disk, the overall appearance of the arms is relatively smooth and unbroken. This is not what is seen in M51. The molecular arm is seen to align with the dust lane (usually taken as the location of the shock) over the majority of the disk (VKS; RK). Also, the clumpy, patchy appearance of the molecular arms indicates that other processes are competing with the orbit crowding to produce the observed appearance of the gas distribution in M51.

Dissipative cloud-cloud collisions allow the model disk to reach a steady state, eliminating the sloshing of the spiral pattern (RS). These collisions are necessary to keep the cloud-to-cloud velocity dispersion in the arms from getting too large (i.e., the gas in the arms will "heat up"), which would wash out the spiral pattern. When self-gravitational effects are added to the simulations, the clumping of clouds on local scales becomes much more pronounced (Adler 1989; Roberts, Lowe, & Adler 1990), giving the arms a globally ordered, locally patchy appearance that resembles the molecular arms of M51.

It should be noted at this point that the models discussed above account for only one phase (molecular) of the ISM. The possibility that a fraction of the molecular gas is dissociated into atomic form by the star formation process downstream from the dust lanes (Allen et al. 1986; Tilanus & Allen 1991) complicates the picture.

The properties of the molecular emission derived in this paper support the results of the *N*-body simulations. The average arm-to-interarm intensity contrasts for the various arm segments ranged from $\geq 3.5:1$ to $\geq 6.3:1$ with an average value of $\geq 4.6:1$. For an *N*-body simulation with a spiral perturbation of $\sim 7\%$ above the axisymmetric potential and dissipative collisions and gaseous self-gravity included, the intensity contrast ranges from 5:1 to 9:1, with an average value of $\sim 6:1$ (Adler 1989; Roberts et al. 1990). Arm widths in the simulation are typically on the order of 1 kpc, in agreement with Figure 4 and the single-dish work of GBG.

The observed velocity dispersions are roughly consistent with those of the *N*-body simulations. The simulations show that for a disk-averaged cloud-cloud velocity dispersion of 6 km s^{-1} in the plane of the galaxy (the disk was kept at this level to ensure disk stability; see RH), the average dispersion values in the arms reached up to 20 km s^{-1}. Since our large linear beam most certainly contains several clouds, our measured velocity dispersions will be indicative of the cloud-to-cloud motions (largely perpendicular to the galactic disk; sec § 4.5). The line widths of the GMAs listed in Table 2 range from 20 to 45 km s^{-1}; this corresponds to velocity dispersions of 7–20 km s^{-1}. These values are in agreement with the models, assuming that the observed dispersions are typical of the dispersions in the disk of M51.

The percentage of emission restricted to the arm regions ($\sim 75\%$ of the emission in $\sim 25\%$ of the area) is higher than that predicted by the numerical models. RS, Roberts et al. (1990), and Adler (1989) find that about 50% of the clouds are found in the region of the spiral arms, which also covered roughly 25% of the disk. Kwan & Valdes (1983, 1987) get very similar values (53% of the emission covering 28% of the area) using cloud coalescence as compared with inelastic collisions. The similarity of these two numerical results which use completely different cloud interaction mechanisms and different procedures to compute the gaseous self-gravity indicate again that the primary mechanism of gathering clouds into the arms is the presence of the spiral density wave. A simple explanation for the high level of gas restriction to the arms in M51 is that the density wave is stronger than the perturbation used in the numerical models. This conclusion is further supported by the fact that the streaming motions (70 km s^{-1}: VKS, RK, this work; 90 km s^{-1} in Hα: Tilanus 1990, Tilanus & Allen 1991) are larger than those seen in the models.

Unfortunately, from the data obtained in the current survey, we are unable to distinguish between the different cloud interaction mechanisms used in the different simulations. Both the inelastic collision method of cloud interaction (RH; RS; Adler 1989) and cloud coalescence (Kwan & Valdes 1983, 1987; Tomisaka 1984, 1986; Combes & Gerin 1986) produce similar results on the linear scale that we are able to investigate. It will take much higher resolution observations to make out the properties of the individual clouds in the GMAs.

5.2. *Role of Spiral Density Waves in Star Formation*

Elmegreen (1987) was among the first to propose that the role of spiral density waves may be merely to concentrate the molecular clouds and does not directly stimulate star formation in molecular clouds. One observational test is to compare the star formation efficiency on and off the arms, where the efficiency may be defined as the ratio of stellar mass to gas mass.

A practical way to do this is to compare the arm-to-interarm contrast in Hα intensity and the contrast in CO intensity. The

TABLE 3

Derived Properties of CO Emission in Two Fields of M51

Parameter	Value
Peak arm-interarm CO intensity contrast	$\geq 20:1$
Average arm-interarm CO intensity contrast	$\geq 4.6:1$
Restriction of CO emission to arms	75% of emission over 25% of area
Molecular spiral arm width	≤ 1.3 kpc
Streaming motions in spiral arm	Up to ± 70 km s^{-1}
GMA sizes	300–800 pc
GMA velocity dispersions[a]	7–20 km s^{-1}
GMA gas masses [$M(H_2) \times 1.36$]	(1–40) $\times 10^7$ $M_\odot$
Spacing of GMAs along arms	1–2 kpc

[a] Largely perpendicular to the disk of M51; $i = 20°$.

assumptions involved are that (1) the Hα flux is proportional to the number of young stars formed (see Lees & Lo 1991); (2) the conversion ratio between CO intensity and H_2 column density is the same everywhere in the galaxy; and (3) molecular gas dominates all other phases. Another practical limitation is the relative extinction of Hα flux on and off the arms. For the extinction there is no direct measurement because of the faintness of the Hα emission from the interarm region. For the conversion ratio there is no direct measurement yet, but there is observational evidence that the gas properties on and off may be different. For example, GBG show that the ^{13}CO ($J = 2$–1)/CO ($J = 2$–1) integrated intensity ratio is different for the arm and interarm regions of M51.

Thus, even though the average CO ($J = 1$–0) arm-to-interarm contrast of $\geq 5:1$ is very close to the Hα contrast (uncorrected for extinction) of 6.4:1 found by Lees & Lo (1990), the relative star formation efficiency on and off the spiral arms is not well known. The role of the spiral density wave in the star formation process, at least in M51, is still not clear.

6. SUMMARY

Interferometer and combined single-dish interferometer maps of two fields in M51 have been presented. The interferometer map recovers from 45% to 55% of the total single-dish flux density, while the combined map recovers most of the flux density.

Inspection of the two maps shows that the majority of the flux density recovered in the combined map lies in the spiral arm regions. While the peaks remain generally the same shape, size, and intensity, the arms become wider and more continuous when compared with the interferometer map. This is consistent with interferometer maps that recover less flux density than BIMA; these maps have narrower arms, leading to the conclusion that the higher the percentage of total flux density recovered, the wider and more continuous the arms appear. Arm widths of up to 1.3 kpc are seen, and the CO arms are clumped on a linear scale of ~ 1 kpc. Several clumps of interarm emission are detected in our combined map, but the majority of the interarm emission falls below the noise level of the map. Only 25% of the total CO flux density is found in the interarm regions.

A summary of the properties derived from the combined map is presented in Table 3. This map shows properties that indicate the presence of spiral density waves. The average arm-to-interarm intensity contrast over the entire field of view is $\geq 4.6:1$. Peak arm-to-interarm intensity contrasts are higher than in previous work in the galaxy, with a lower limit of 20:1. The inner arms show higher intensity contrasts than the outer arms, indicating that the spiral shock is stronger in the inner regions. The results are consistent with other high-resolution studies of the galaxy as well as single-dish studies of galaxies where the interarm regions can be resolved. Plots of I_{CO} versus azimuthal angle at various galactocentric radii show that the CO arms are quite well defined. Streaming motions of up to 70 km s^{-1} (in the plane of the galaxy), in a direction consistent with density wave theory, are seen in the arms.

These results are consistent with numerical models that show that the primary mechanism of cloud gathering in the spiral arms is orbit crowding (caused by the presence of a density wave). The clumpiness of the CO emission along the spiral arm suggests that dissipative cloud-cloud collisions and gaseous self-gravity may also play a role.

This work was supported in part by NSF grants 87-15905 and by the Laboratory for Astronomical Imaging at the University of Illinois. Wolfgang Batrla helped in the early stages of the reduction of the combined maps. We would like to thank Rob Kennicutt, Joanna Lees, William Roberts, and Frank Shu for useful discussions.

REFERENCES

Adler, D. S. 1989, Ph.D. thesis, Univ. Virginia
Adler, D. S., Lo, K. Y., & Allen, R. J. 1990, in The Interstellar Medium in External Galaxies, ed. D. J. Hollenbach & H. A. Thronson (NASA CP-3084), 291
Allen, R. J., Atherton, P. D., & Tilanus, R. P. J. 1986, Nature, 319, 296
Allen, R. J., & Goss, W. M. 1979, A&AS, 36, 135
Bahcall, J. N. 1984, ApJ, 276, 169
Cohen, R. S., Dame, T. M., Garay, G., Montani, J., Rubio, M., & Thaddeus, P. 1988, ApJ, 331, L95
Combes, F., & Gerin, M. 1986, A&A, 150, 327
Dame, T. M., Elmegreen, B. G., Cohen, R. H., & Thaddeus, P. 1986, ApJ, 305, 892
Elmegreen, B. G. 1987, in Star Forming Regions, ed. M. Peimbert & J. Jugaku (Dordrecht: Reidel), 457
Garcia-Burillo, S., & Guélin, M. 1990, in IAU Symp. 146, Dynamics of Galaxies and Molecular Cloud Distributions, ed. F. Casoli & F. Combes (Dordrecht: Kluwer), 67 (GBG)
Guélin, M., Garcia-Burillo, S., Blundell, R., Cernicharo, J., Despois, D., & Steppe, H. 1989, Highlights Astron., 8, 575 (G89)
Johansson, L. E. B. 1990, in IAU Symp. 146, Dynamics of Galaxies and Molecular Cloud Distributions, ed. F. Casoli & F. Combes (Dordrecht: Kluwer), 1
Kwan, J., & Valdes, F. 1983, ApJ, 271, 604
———. 1987, ApJ, 315, 92
Lees, J. F., & Lo, K. Y. 1990, in The Interstellar Medium in External Galaxies, ed. D. J. Hollenbach & H. A. Thronson (NASA CP-3084), 296
———. 1991, ApJ, submitted
Lo, K. Y. 1991, in Proc. Third Haystack Observatory Meeting, Skylines, ed. A. D. Haschick & P.T. P. Ho (Provo: ASP), 7

Lo, K. Y., Ball, R., Masson, C. R., Phillips, T. G., Scott, S., & Woody, D. P. 1987, ApJ, 317, L63 (L87)
Lo, K. Y., Tilanus, R. P. J., Allen, R. J., Wright, M. C. H., & Jackson, J. 1989, in Proc. UMASS Conf. on Molecular Clouds in the Milky Way and External Galaxies, ed. J. Dickman, R. Snell, & J. Young (Berlin: Springer-Verlag), 439
MacLaren, I., Richardson, K. M., & Wolfendale, A. W. 1988, ApJ, 333, 821
Maloney, P. M. 1990, in The Interstellar Medium in Galaxies, ed. H. A. Thronson & J. M. Shull (Dordrecht: Kluwer), 493
Mundy, L. G., Scoville, N. Z., Bååth, L. B., Masson, C. R., & Woody, D. G. 1986, ApJ, 304, L51
Planesas, P., Scoville, N. Z., & Myers, S. T. 1991, ApJ, 369, 364
Rand, R. J., & Kulkarni, S. R. 1990, ApJ, 349, L43 (RK)
Rickard, L. J., & Palmer, P. 1981, A&A, 102, L13
Roberts, W. W. 1969, ApJ, 158, 123
Roberts, W. W., & Adler, D. S. 1989, Celest. Mech., 45, 285
Roberts, W. W., & Hausman, M. A. 1984, ApJ, 277, 144 (RH)
Roberts, W. W., Lowe, S. A., & Adler, D. S. 1990, in Ann. NY Acad. Sci., No. 596, Galactic Models, ed. J. R., Buchler, S. T. Gottesman, & J. H. Hunter (New York: NY Acad. Sci.), 130
Roberts, W. W., & Stewart, G. R. 1987, ApJ, 314, 10 (RS)
Rubio, M., Garay, G., Montani, J., & Thaddeus, P. 1991, ApJ, 368, 173
Rydbeck, G., Hjalmarson, Å., & Rydbeck, O. E. H. 1985, A&A, 144, 282 (RHR)
Rydbeck, G., Hjalmarson, Å., Wilkind, T., & Rydbeck, O. E. H. 1989, in Proc. UMASS Conf. on Molecular Clouds in the Milky Way and External Galaxies, ed. J. Dickman, R. Snell, & J. Young (Berlin: Springer-Verlag), 446 (RHWR)
Sanders, D. B., & Scoville, N. Z. 1984, ApJ, 276, 182
Scoville, N. Z. & Sanders, D. B. 1987, in Interstellar Processes, ed. D. J. Hollenbach & H. A. Thronson (Dordrecht: Reidel), 21
Scoville, N. Z., & Young, J. S. 1983, ApJ, 265, 148
Scoville, N. Z., Yun, M. S., Clemens, D. P., Sanders, D. B., & Waller, W. H. 1987, ApJS, 63, 821
Solomon, P. M., Rivolo, A. R., Barrett, J., & Yahil, A. 1987, ApJ, 319, 730
Stark, A. A. 1985, in IAU Symp. 106, The Milky Way Galaxy, ed. H. van Woerden, R. J. Allen, & W. B. Burton (Dordrecht: Reidel), 445
Thompson, A. R., Moran, J. M., & Swenson G. W. 1986, Interferometer and Synthesis in Radio Astronomy (New York: Wiley)
Tilanus, R. P. J. 1990, Ph.D. thesis, Groningen
Tilanus, R. P. J., & Allen, R. J. 1989, ApJ, 339, L57
———. 1991, A&A, in press
Tomisaka, K. 1984, PAS, 36, 457
———. 1986, PAS, 38, 95
Tully, R. B. 1974, ApJS, 27, 437
Verter, F., & Kutner, M. L. 1988, Lecture Notes in Physics, Vol. 306, The Outer Galaxy, ed. L. Blitz & F. J. Lockman (Berlin: Springer-Verlag), 253
Visser, H. C. D. 1980a, A&A, 88, 149
———. 1980b, A&A, 88, 159
Vogel, S. N., Kulkarni, S. R., & Scoville, N. Z. 1988, Nature, 334, 402 (VKS)
Vogel, S. N., Wright, M. C. H., Plambeck, P. L., & Welch, W. J. 1984, ApJ, 283, 655
Wilson, C. D. & Scoville, N. Z. 1990, ApJ, 363, 435